Title here

Elio Campitelli * and Leandro Díaz

CIMA UBA blablabla

Carolina Vera

Corresponding author: Elio Campitelli,elio.campitelli@cima.fcen.uba.ar

ABSTRACT

Enter the text of your abstract here. This is a sample American Meteorological Society (AMS) LaTeX template. This document provides authors with instructions on the use of the AMS LaTeX template. Authors should refer to the file amspaper.tex to review the actual LaTeX code used to create this document. The template.tex file should be modified by authors for their own manuscript.

Significance statement. This is significant becasue I wrote it.

1. Introduction

yada yada SAM yada yada circulation.. yada yada so important. yada yada many impacts.

2. Methods

1) DATA

We used monthly geopotential height at 2.5 longitude by 2.5 latitude resolution from ERA5 (Hersbach et al.) for the period 1979 to 2018 (inclusive).

Monthly temperature NOAA Global Surface Temperature (NOAAGlobalTemp) 5.0 degree latitude x 5.0 degree longitude global grid (Vose et al. 2012; Smith et al. 2008). The same analysis was carried out using CRUTEM4 (Osborn and Jones 2014) (not shown).

We used monthly precipitation data from CPC Merged Analysis of Precipitation (Xie and Arkin 1997) 2.5 degree latitude x 2.5 degree longitude.

2) DEFINITION OF INDICES

We defined the Southern Annular Mode (SAM) as the leading EOF of the monthly anomalies of geopotential field at 700 hPa south of 20°S (citation?). The EOF was performed by computing the Singular Value Decomposition of the data matrix consisting in 481 rows and 4176 columns (144 points of longitude and 29 points of latitude). The values where weighted by the square root of the cosine of latitude to account for the non-equal area of each gridpoint (Chung and Nigam 1999). This same method was used at the rest of the levels considered in this paper.

To separate between the zonally symmetric and asymmetric components of the SAM, we computed the zonal mean and anomalies of the full SAM spatial pattern. The results are shown in

Figure 3 for 700hPa. The full spatial signal ($\mathrm{EOF}_1(\lambda,\phi)$) is the sum of the zonally asymmetric ($\mathrm{EOF}_1^*(\lambda,\phi)$) and symmetric ($[\mathrm{EOF}_1](\lambda,\phi)$) components. We then compute the "Full", "Asymmetric" and "Symmetric" indices, by regressing each geopotential field on these patterns (weighting by the cosine of latitude).

The three indices are normalised by dividing them by the standard deviation of the "Full" index at each level. This means that comparing the magnitude between indices is meaningful, but it also means that not every index will have unit standard deviation.

3) Significance

We adjusted p-values for False Detection Rate following Wilks (2016).

3. Results

a. Temporal evolution

Figure 4 shows the resulting Asymmetric and Symmetric time series corresponding to 700 and 30hPa. blablababla #FIXME

- stratosphere clearly nor normally distributed. a lot of values near 0 and some relatively high outliers. Especially true int he case of the asymmetric index. High frequency variablity.
- In both levels, there's correlation between the series (expected),

Correlations between the Asymmetric and Symmetric series are rather constant throught the troposphere, fluctiating between 0.39 and 0.45 (Figure 5). Futhermore, the cross-correlation of each series across levels –shown in Figure 6– are high in the trosposphere (greater than 0.9) for both indices. This suggests that both the Asymmetric and the Symemtric component of the tropospheric SAM are highly vertically coherent, both in their individual evolution and their

temporal relationship. This is to be expected since the SAM is mostly equivalent barotropic (citaaaa).

In the stratosphere the situation is different. As can be seen in Figure 5, the relationship between the Asymmetric and Symmetric indices varies with height above 100 hPa. It starts to decreese right over the tropopause, reaches a minium of 0.21 at 20 hPa and then it increases again monotonically with height up to the uppermost level of the reanalysis. The cross-correlation across levels in the stratosphere is generally weaker than in the troposphere (Figure 6). Furthermore, above 100 hPa, the cross-correlation decreases more rapdily with height for the Symmetric SAM than for the Asymmetric SAM as evidenced by the wider dark red areas near the diagonal in Figure 6b) vs. Figure 6c). Moreover, the stratospheric Symmetric SAM seems to be slightly more connected to the trosposphere than the Asymmetric SAM; this can be seen by the lower correlation values in the top right quadrant of Figure 6b) in comparison with Figure 6c).

Figure 6a) show the cross-correlation across levels for the Full SAM index. #FIXME

Figure 7 shows normalised decadal trends for each index for the whole period along with a 95% interval in shading. There is a statistically significant increase in positive SAM in the tropostphere (panel a), which has been already documented in other studies (e.g. Fogt and Marshall (2020)). Panels b and c of Figure 7 show that this increase is evident only in the Symmetric component. This distinction should prove useful when attributing trends in other variables such as temperature and precipitation to trends in the SAM.

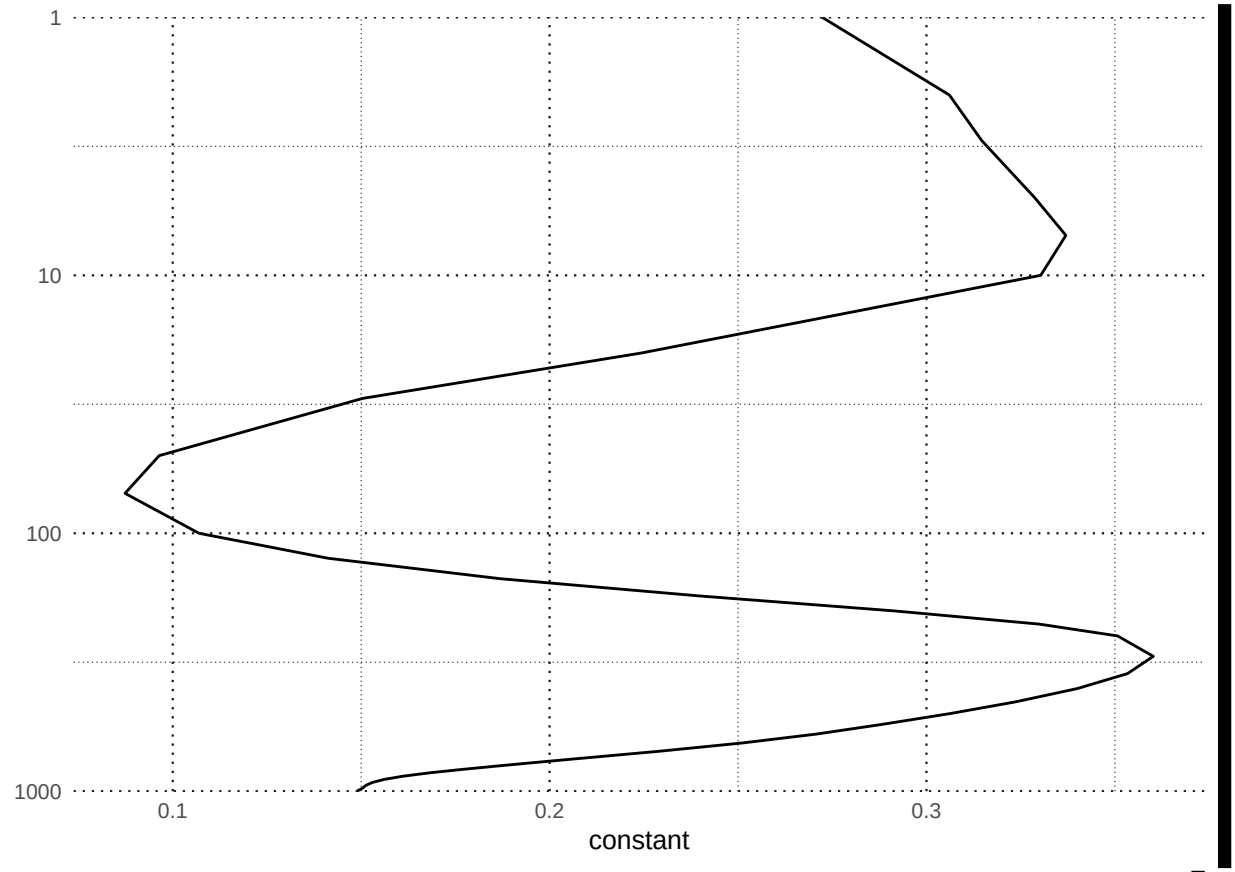
1
10
100
1000
0.1
0.2
0.3
constant

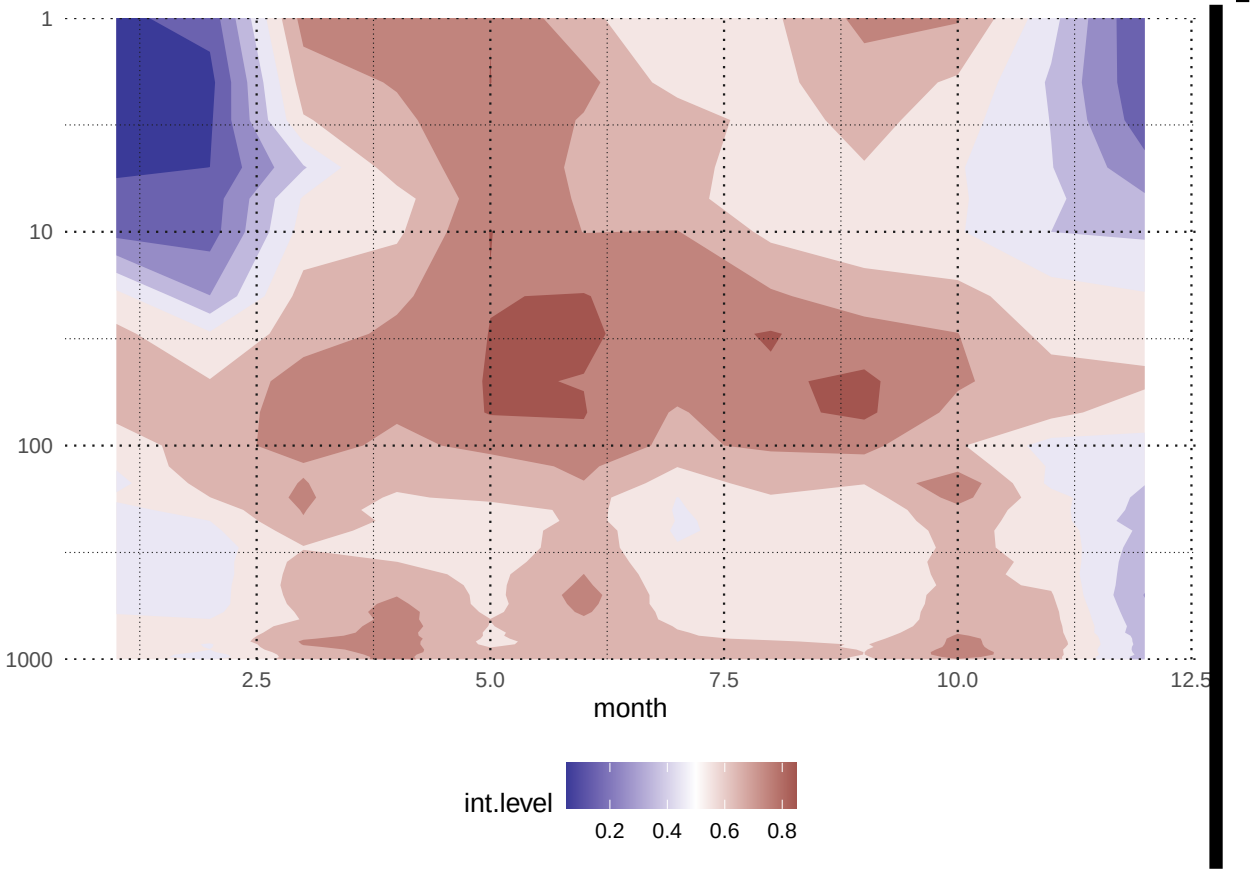
1
10
100
1000
2.5
5.0
7.5
10.0
12.5
month
int.level
0.2
0.4
0.6
0.8

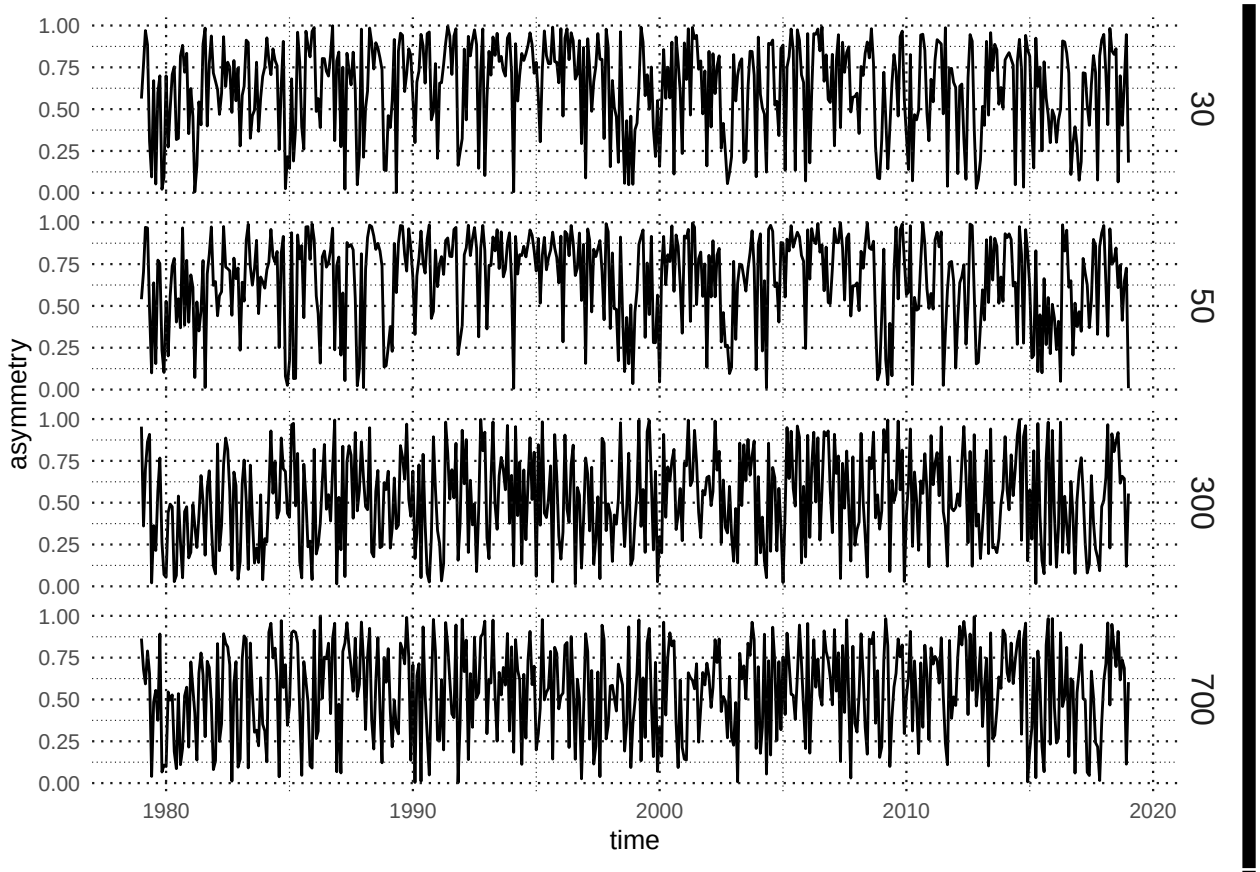
asymmetry
1.00
0.75
0.50
0.25
0.00
30
50
300
700
1980
1990
2000
2010
2020
time

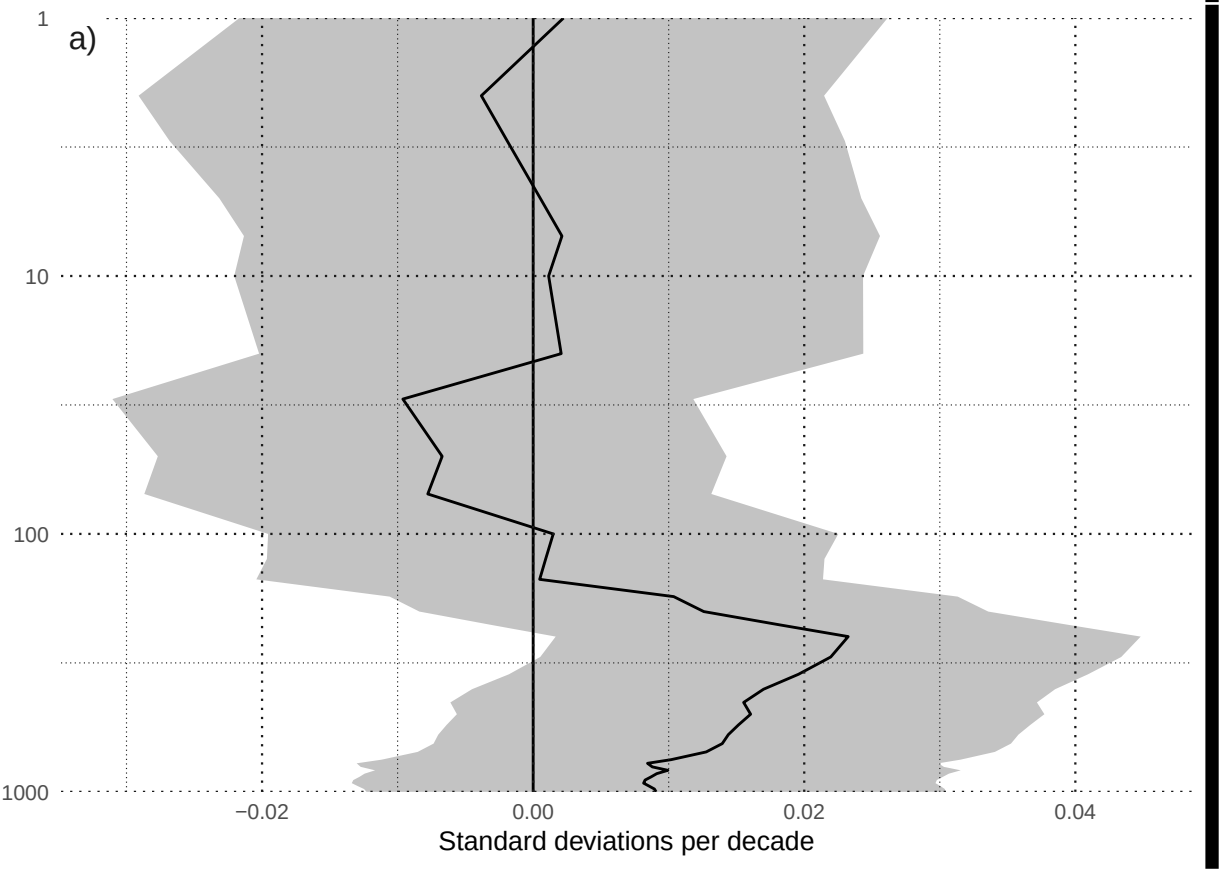
a)
1
10
100
1000
−0.02
0.00
0.02
0.04
Standard deviations per decade

b. Spatial patterns

To undertand the spatial patterns associated with both indeces, we regressed monthly geopotential anomalies into both indeces using multiple regression (Figure A6 illustrates the difference between computing two simple regressions and one multiple regression).

Figure 8 shows the spatial year-long regression for selected levels. In the troposphere the Full annular mode is clearly "contaminated" with well known zonal asymemtries (panels g and j) which are succesfully sepparated by our methodology (panels h, i, k and l). In the stratosphere, the spatial pattern associated with the Full SAM is much more clearly dominated by a zonally symmetric, monopolar structure (panels a and d) that is, however, not perfectly centered in the south pole. The monopoloe obtained by multiple regression with the Asymmetric and Symmetric SAM (panels c and f in Figure 8) is much more symmetric and the shift from total symmetry is captured by the regression pattern of the Asymmetric SAM as a wave-1 pattern (panels b and e).

The amplitude of each zonal wave number at each latitude at 50 hPa and 700 hPa is shown in Figure 9, where wave number zero represents the zonal mean. Comparing between rows, this Figure quantifies the relatively clean separation between the zonally symmetric and zonally asymmetric structures, as its evident how the mixture of waves of the Full field (first row) is very similar to the sum of the waves of the Asymmetric and Symmetric field (second and third row, respectively). The second row of Figure 9 shows that the Asymmetric SAM is overwhelmingly dominated by wave 1 in the stratosphere (panel b), while in the stratosphere it is composed of zonal waves 3 to 1 in decreasing level of importance.

From Figure 8 it appears that the vertical structure of the Asymmetric SAM is equivalent barotropic in the troposphere but baroclinic in the stratosphere. Anomalies are centerd in the same locations in the troposphere (panels h and k), but show westerly displacement in the stratosphere

(panesl b and e). This is expanded in Figure 10, which shows a vertical crossection of the regression coefficient corresponding to the middle row of Figure 8, area-weighted averaged between 65 and 40 degrees South. Below 100 hPa, anomalies are completely vertical, while above they show an important westerly tilt with height.

c. Impacts

1) Temperature

Figure 1 shows regression coefficients of each index at 700 hPa with surface temperature for each trimester. It is evident that the Asymmetric and Symmetric SAM indices are associated with overall distinct temperature patterns which can be obscured when using the Full SAM index. The Symmetric SAM signal is weaker than the Asymmetric SAM, as evidenced by the relatively smaller and les sstatistically significant regression coefficients in row 3 of Figure 1 compared with row 2.

In DJF (column a), the strong negative signal in the tropical Pacific in panel a.1 is mostly associated with the Asymmetric component (panel a.2), as is it largely absent in the Symmetric component (panel a.3). Furthermore, the Asymmetric SAM is also asociated with low temperature anomalies in the Indian ocean, but this signal is obscured by the Symmetric variability and thus lost in the Full SAM. Over the continents, the Asymmetric SAM is assoiated with negative temperature anomalies which, again, mostly disappear in the Full SAM regression.

The patterns seen in MAM and JJA (columns b and c) are not robustly significant in the sense that there are no areas with p-values below 0.05 when controlling for FDR following Wilks (2016). Nevertheless, it is interesting to note that in both trimesters, the sign of the regression is consistently flipped between the Asymmetric and Symmetric regressions. In South America, for example, the Asymmetric SAM is associated with positive temperature anomalies in MAM and negative temperature anomales in JJA, while the oposite is the case for the Symemtric SAM.

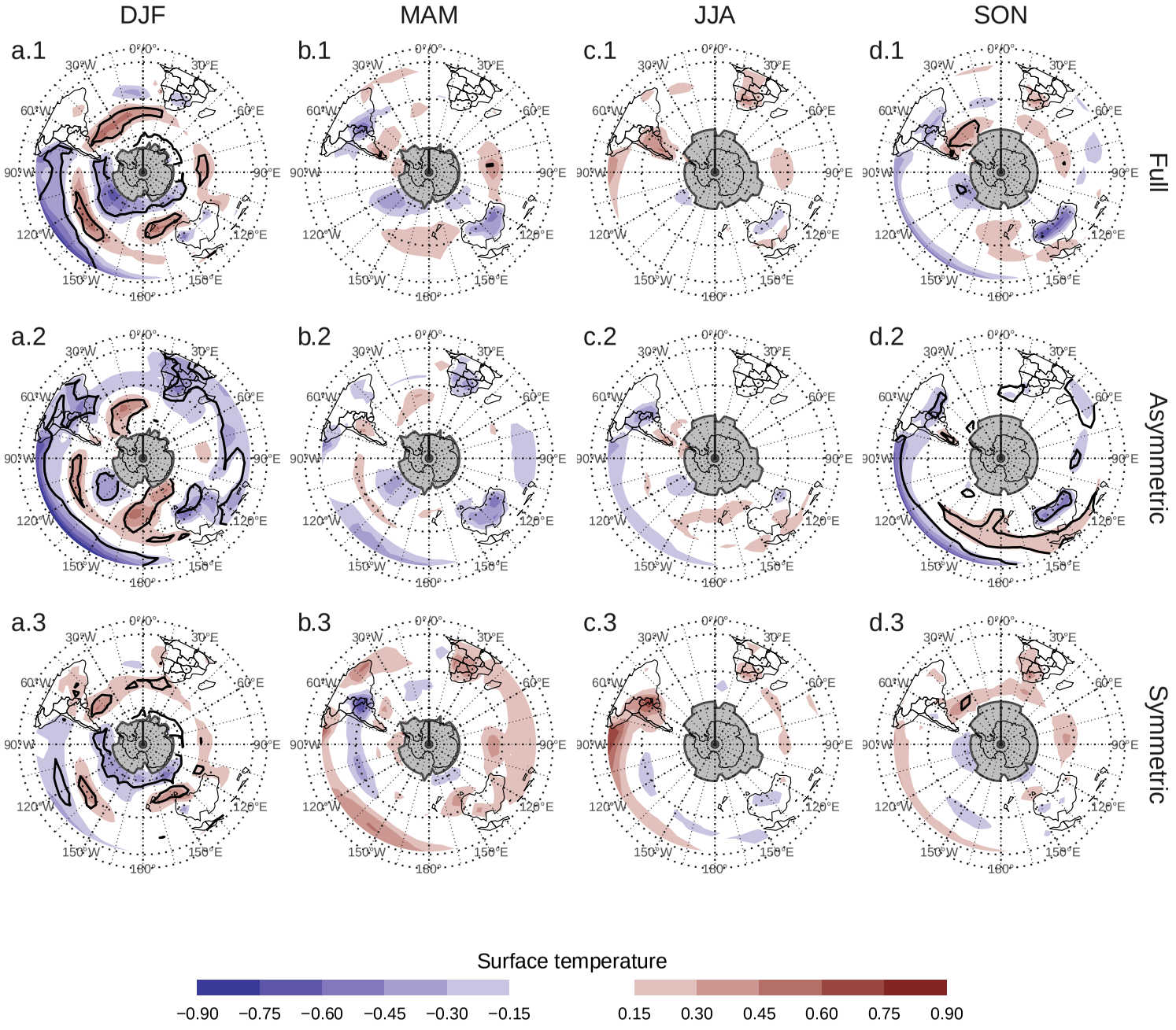

FIG. 1. Regression pattern of surface temperature with Asymmetric and Symmetric SAM. P-values smaller than 0.05 (controlling for Flase Detection Rate) as hatched areas. Gray areas have more than 15% of missing data.

Finally, in SON (column d), there is no significant temperature signal associated with the Symmetric SAM (panel d.3), while the Asymmetric SAM shows a relatively robust signal in the equatorial Pacitic, Australia, and even Southeast South America. This strong signals are reduced in intensity in panel a.3.

2) Precipitation

Acknowledgments. CMAP Precipitation data provided by the NOAA/OAR/ESRL PSL, Boulder, Colorado, USA, from their Web site at https://psl.noaa.gov/

NOAA Global Surface Temperature (NOAAGlobalTemp) data provided by the NOAA/OAR/ESRL PSL, Boulder, Colorado, USA, from their Web site at https://psl.noaa.gov/

References

Chung, C., and S. Nigam, 1999: Weighting of geophysical data in Principal Component Analysis. *Journal of Geophysical Research: Atmospheres*, **104 (D14)**, 16 925–16 928, doi: 10.1029/1999JD900234.

Fogt, R. L., and G. J. Marshall, 2020: The Southern Annular Mode: Variability, trends, and climate impacts across the Southern Hemisphere. *WIREs Climate Change*, **11 (4)**, e652, doi: 10.1002/wcc.652.

Hersbach, H., and Coauthors, ????: The ERA5 global reanalysis. *Quarterly Journal of the Royal Meteorological Society*, **n/a (n/a)**, doi:10.1002/qj.3803.

Osborn, T. J., and P. D. Jones, 2014: The CRUTEM4 land-surface air temperature data set: Construction, previous versions and dissemination via Google Earth. *Earth System Science Data*, **6 (1)**, 61–68, doi:10.5194/essd-6-61-2014.

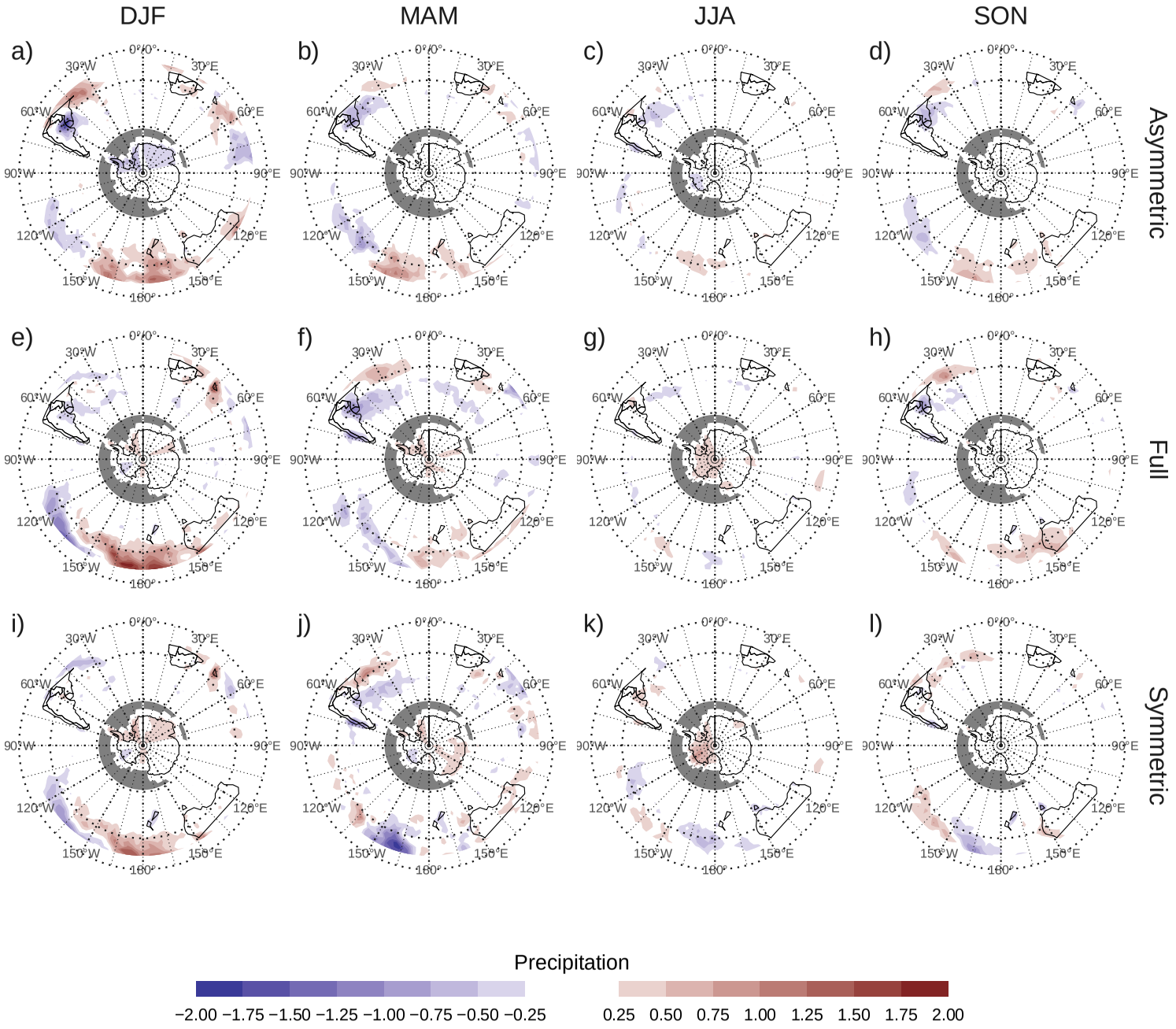

FIG. 2. Regression pattern of precipiation with Asymmetric and Symmetric SAM. P-values smaller than 0.05 (controlling for Flase Detection Rate) as hatched areas.

Smith, T. M., R. W. Reynolds, T. C. Peterson, and J. Lawrimore, 2008: Improvements to NOAA's Historical Merged Land–Ocean Surface Temperature Analysis (1880–2006). *J. Climate*, **21 (10)**, 2283–2296, doi:10.1175/2007JCLI2100.1.

Vose, R. S., and Coauthors, 2012: NOAA's Merged Land–Ocean Surface Temperature Analysis. *Bull. Amer. Meteor. Soc.*, **93 (11)**, 1677–1685, doi:10.1175/BAMS-D-11-00241.1.

Wilks, D. S., 2016: "The Stippling Shows Statistically Significant Grid Points": How Research Results are Routinely Overstated and Overinterpreted, and What to Do about It. *Bull. Amer. Meteor. Soc.*, **97 (12)**, 2263–2273, doi:10.1175/BAMS-D-15-00267.1.

Xie, P., and P. A. Arkin, 1997: Global Precipitation: A 17-Year Monthly Analysis Based on Gauge Observations, Satellite Estimates, and Numerical Model Outputs. *Bull. Amer. Meteor. Soc.*, **78 (11)**, 2539–2558, doi:10.1175/1520-0477(1997)078<2539:GPAYMA>2.0.CO;2.

APPENDIX

Extra figures

LIST OF FIGURES

Fig. 1. Regression pattern of surface temperature with Asymmetric and Symmetric SAM 10

Fig. 2. Regression pattern of precipiation with Asymmetric and Symmetric SAM 12

Fig. 3. Spatial patterns of the first EOF of 700 hPa geopotential height 16

Fig. 4. Time series for the asymmetric SAM and symmetric SAM 17

Fig. 5. Correlation between the Symmetric and Asymmetric SAM at each level 18

Fig. 6. Cross correlation between levels of the Full, Asymmetric and Symmetric SAM 19

Fig. 7. Trends for each index at each level 20

Fig. 8. Regression patterns of geopotential height at 30, 300 and 700 hPa with the Full, Asymmetric and Symmetric SAM 21

Fig. 9. Planteray wave amplitude for the regression patterns at 50 and 700 hPa 22

Fig. 10. Asymmetric coefficient of the multiple regression of mean monthly geopotential height anomalies between 65 and 40 South 23

Fig. A1. Lag-correlation between Symmetric and Asymmetric SAM at each level. 24

Fig. 11. Cross-correlation functions for each index and two differnet base levels 25

Fig. A2. Fourier spectrum of each timeseries. The shading indicates de 95% area derived by fitting an AR process to each series and bootstrapping 5000 simulated samples. 26

Fig. A3. Autocorrelation functions of each timeseries 27

Fig. A5. Regression pattern of precipiation with Asymmetric and Symmetric SAM. P-values smaller than 0.05 (controlling for Flase Detection Rate) as hatched areas. 28

Fig. A6. Regressions maps resulting from performing one multiple regression (a. and b.) and from performing two simple regressions (c. and d.) 29

Fig. A7. 30

Fig. A8. Decadal trends of SAM indices for each season. 31

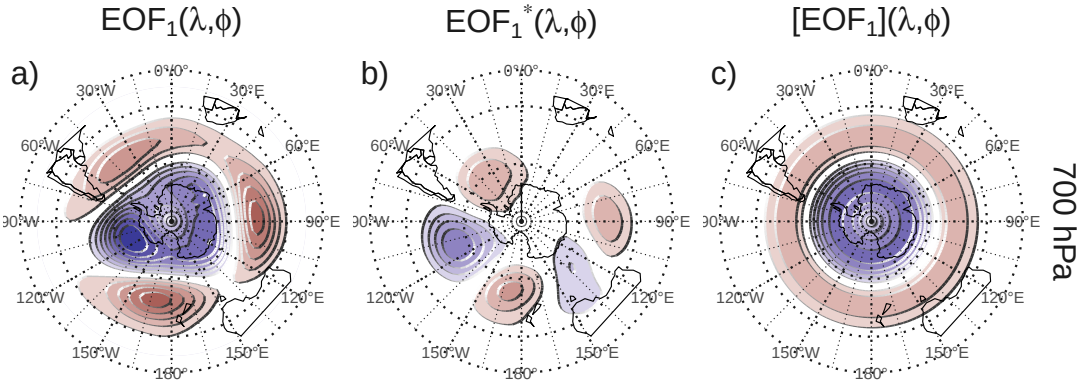

183 FIG. 3. Spatial patterns of the first EOF of 700 hPa geopotential height. Full field (left), zonally asymmetric
184 component (middle) and zonally symmetric component (right). Arbitrary units.

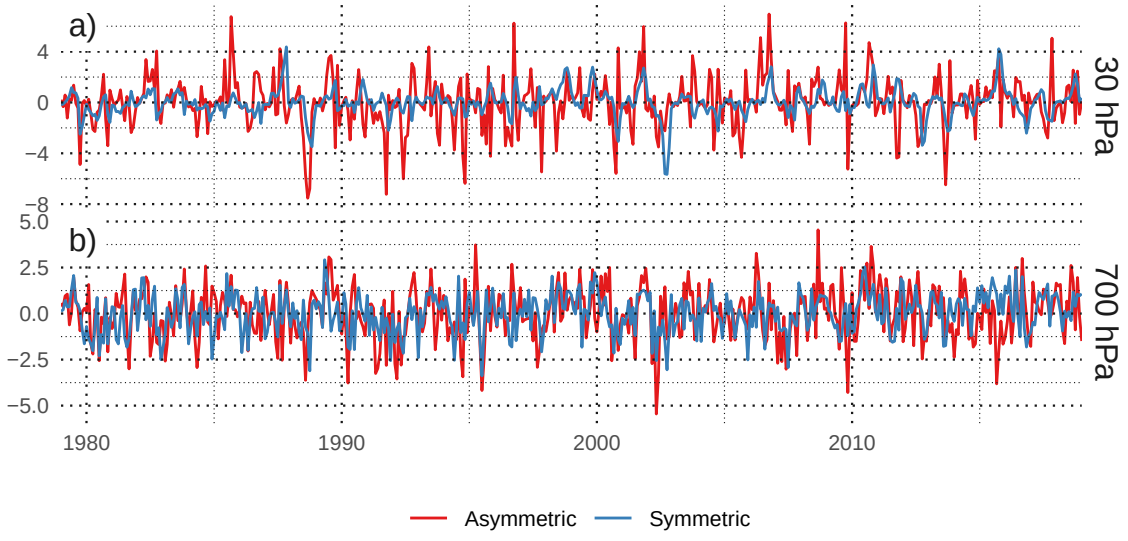

FIG. 4. Time series for the asymmetric SAM and symmetric SAM.

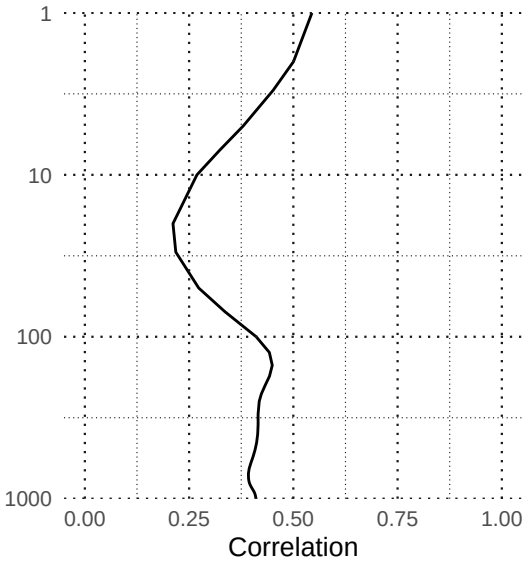

FIG. 5. Correlation between the Symmetric and Asymmetric SAM at each level.

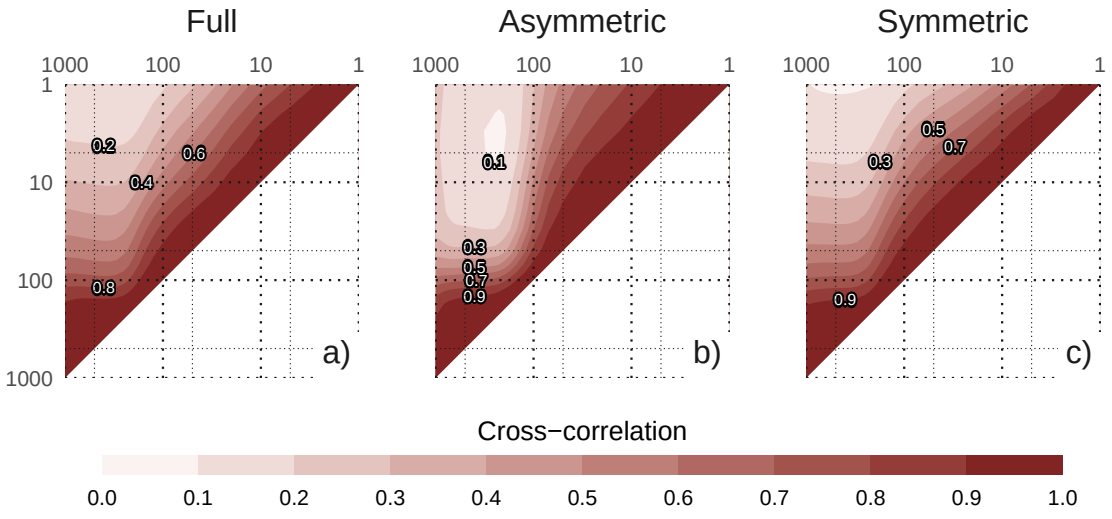

FIG. 6. Cross correlation between levels of the Full, Asymmetric and Symmetric SAM.

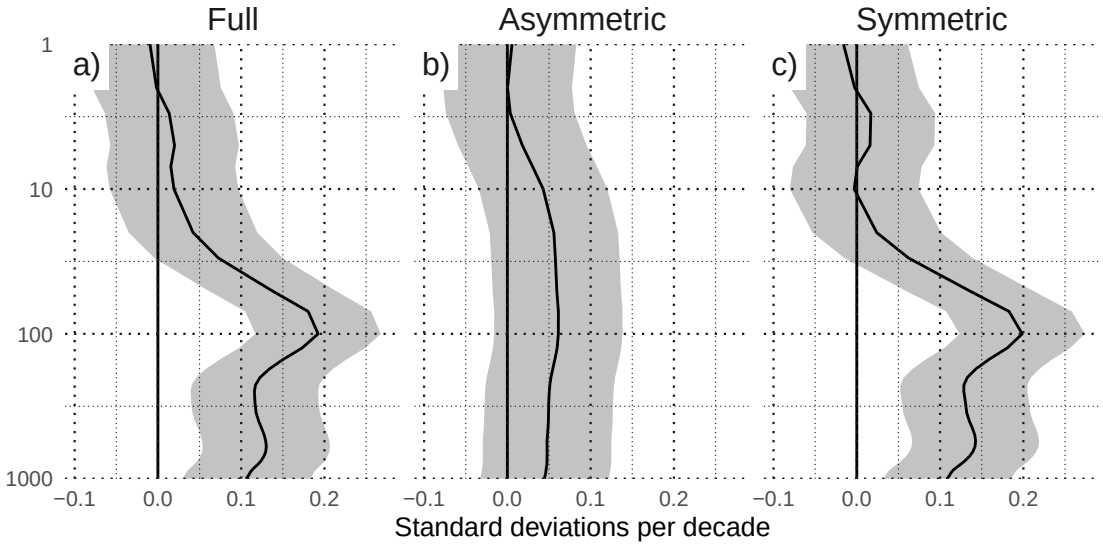

FIG. 7. Trends for each index at each level. Shading indicates the 95% confidence interval.

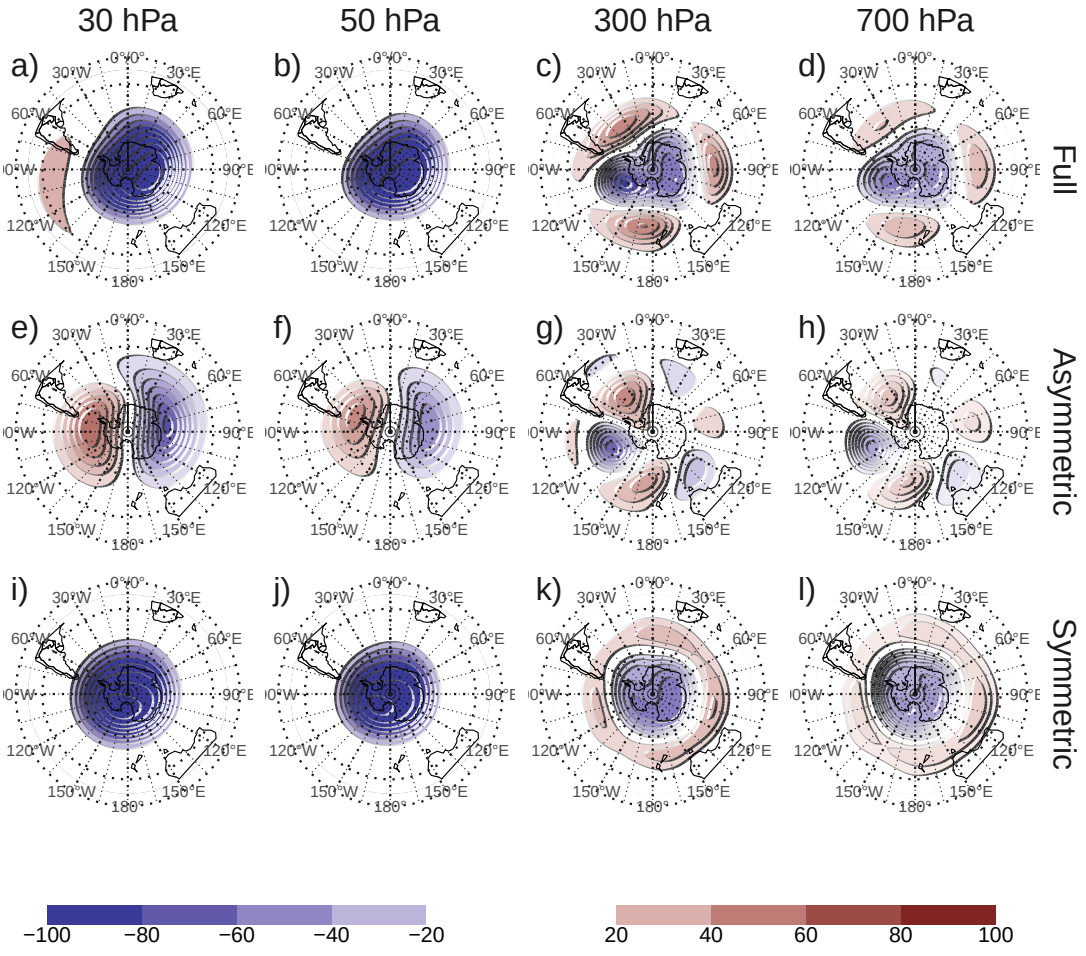

FIG. 8. Regression patterns of geopotential height at 30, 300 and 700 hPa with the Full, Asymmetric and Symmetric SAM. The regression patterns for Asymmetric and Symmetric SAM are the result of one multiple regression using both indices, not of two simple regressions involving each index by itsef.

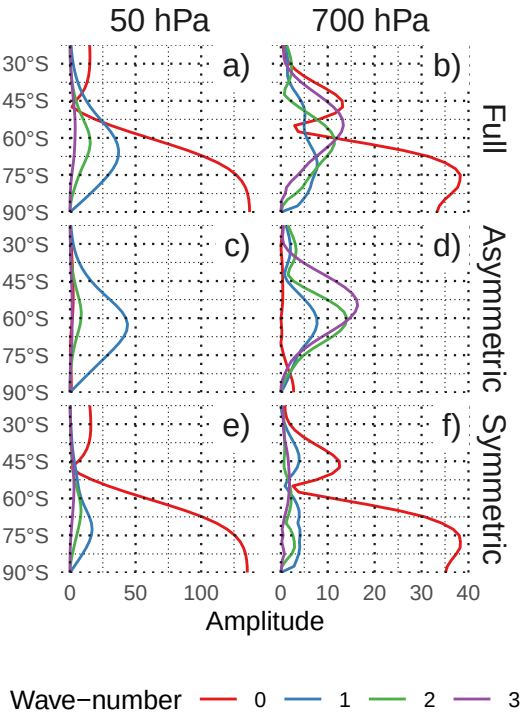

FIG. 9. Planteray wave amplitude for the regression patterns at 50 and 700 hPa.

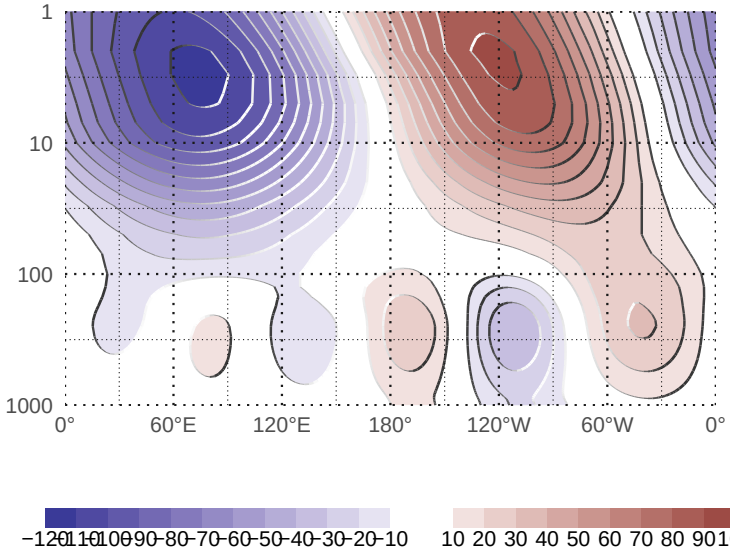

FIG. 10. Asymmetric coefficient of the multiple regression of mean monthly geopotential height anomalies between 65 and 40 South. (this caption needs some love)

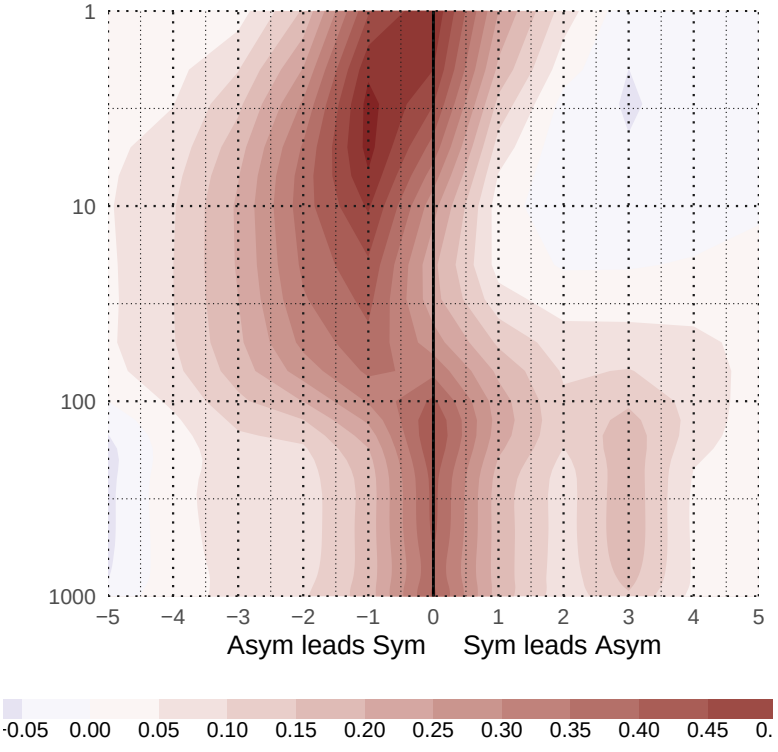

Fig. A1. Lag-correlation between Symmetric and Asymmetric SAM at each level.

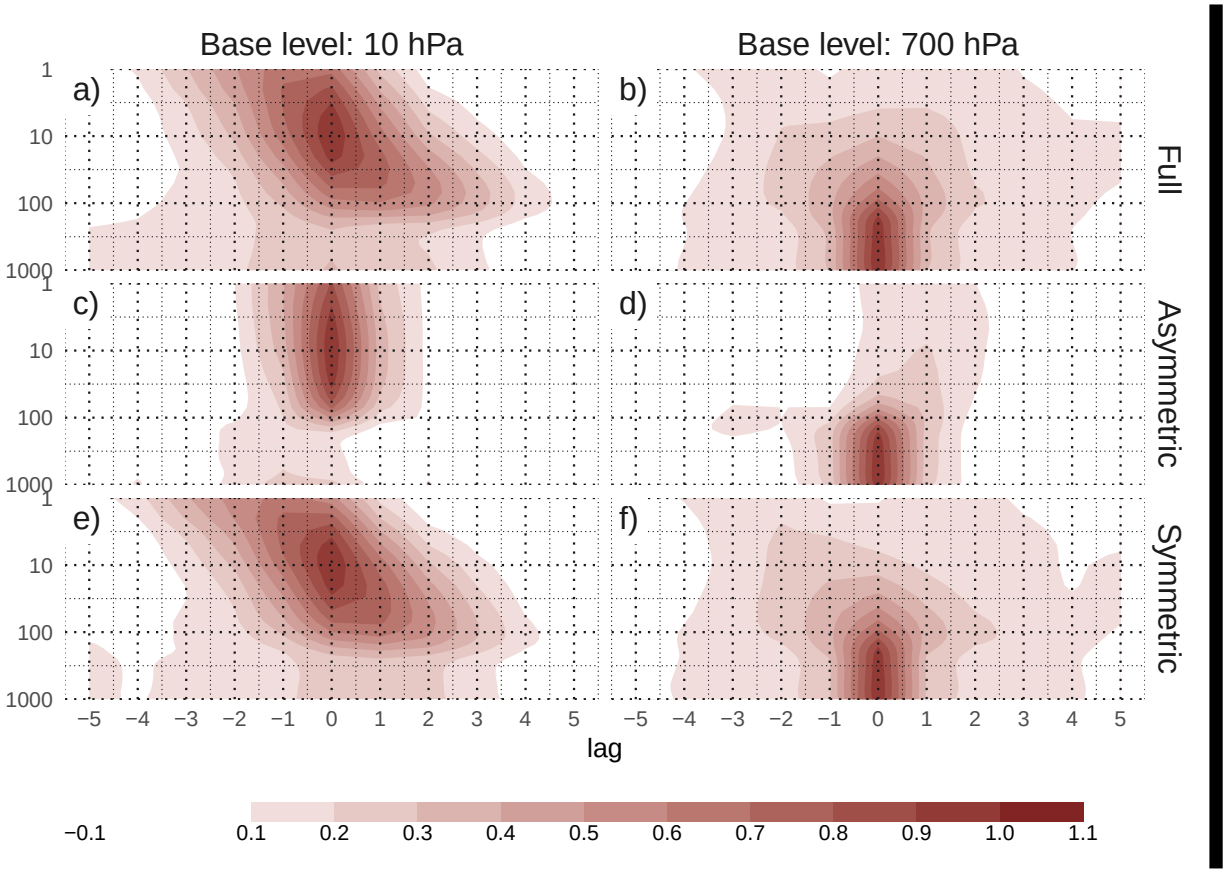

FIG. 11. Cross-correlation functions for each index and two differnet base levels.

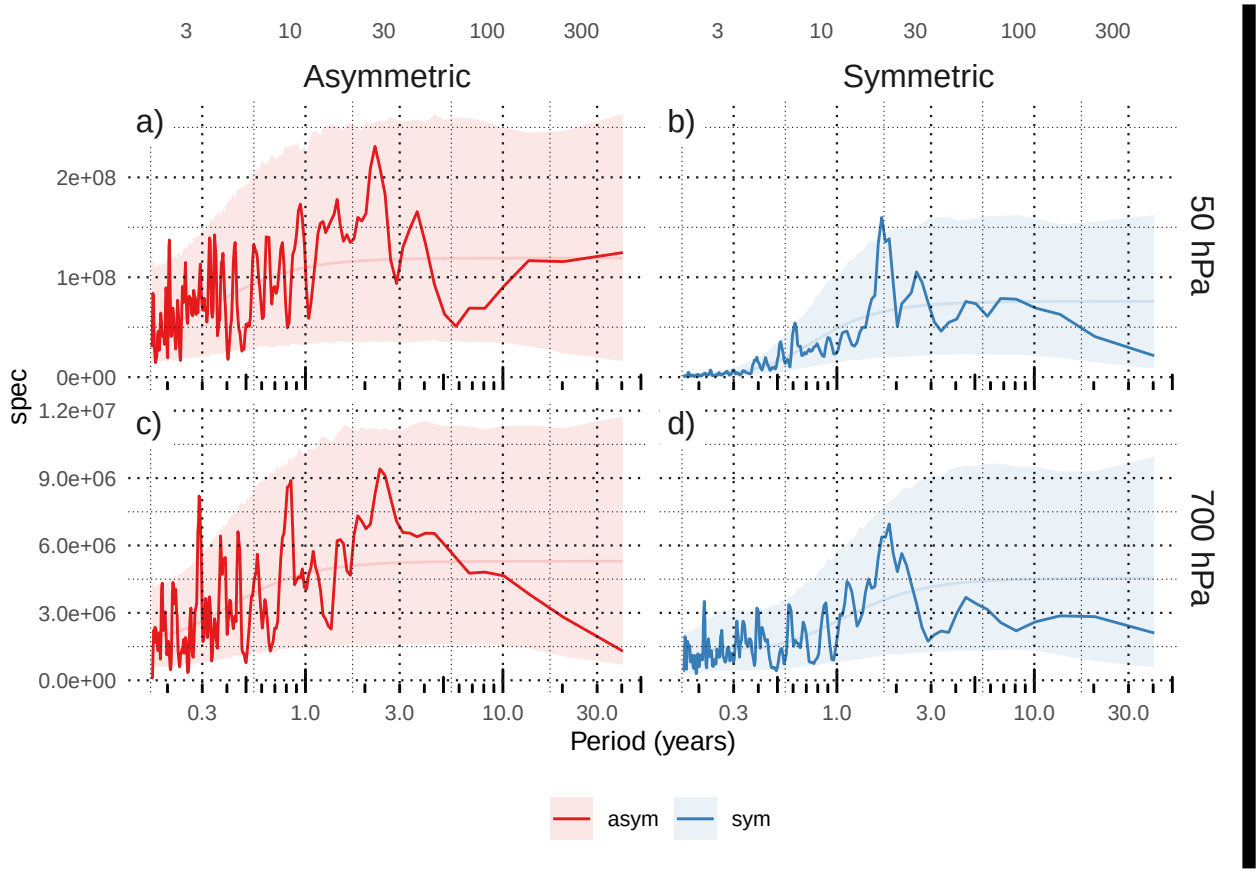

Fig. A2. Fourier spectrum of each timeseries. The shading indicates de 95% area derived by fitting an AR process to each series and bootstrapping 5000 simulated samples.

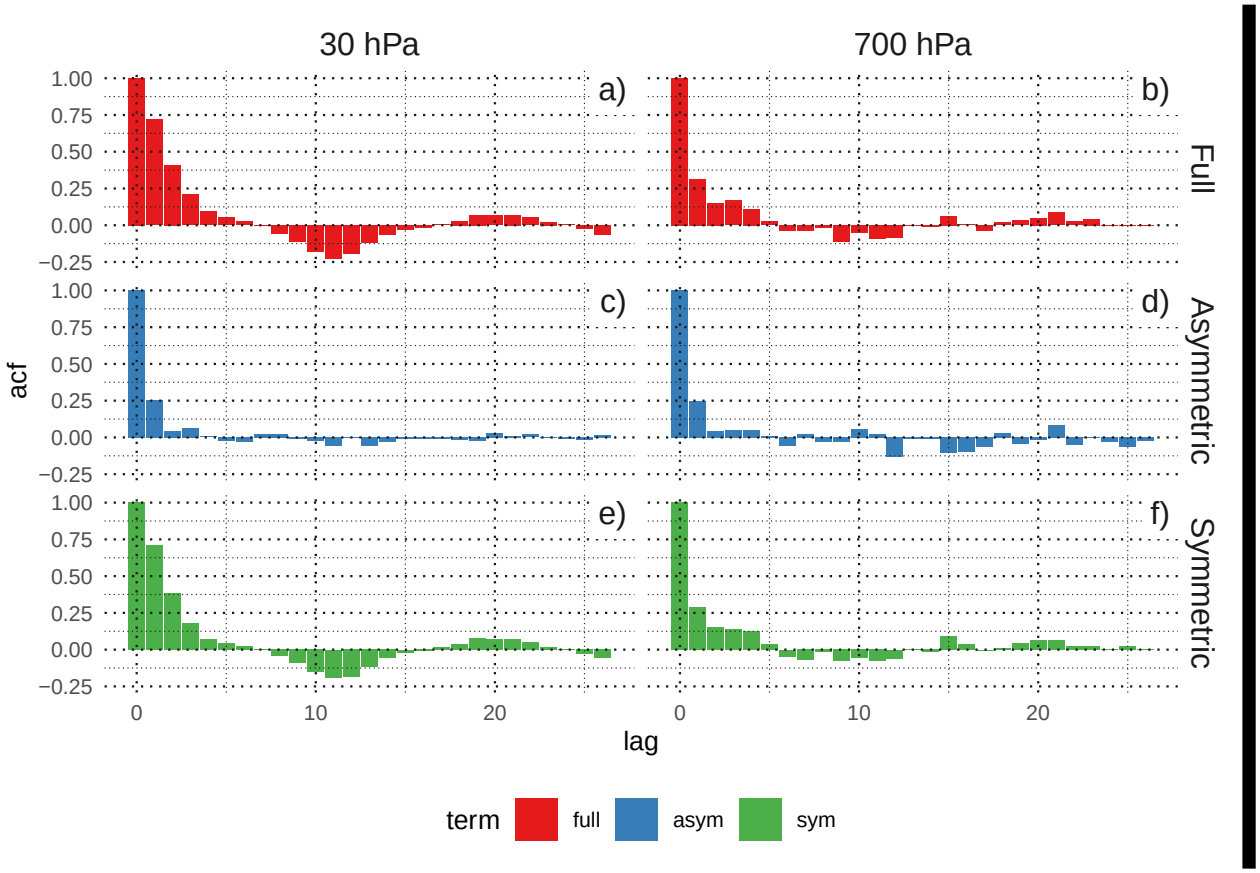

Fig. A3. Autocorrelation functions of each timeseries

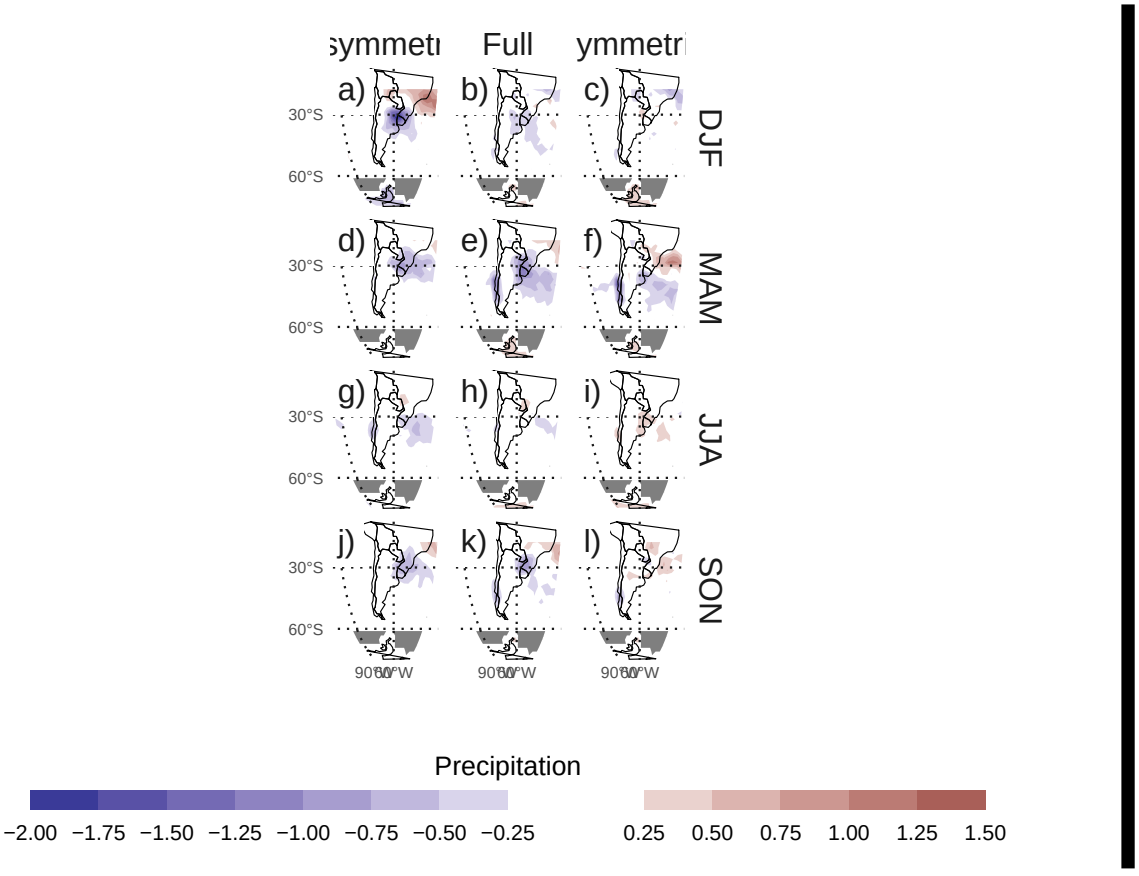

Fig. A5. Regression pattern of precipiation with Asymmetric and Symmetric SAM. P-values smaller than 0.05 (controlling for Flase Detection Rate) as hatched areas.

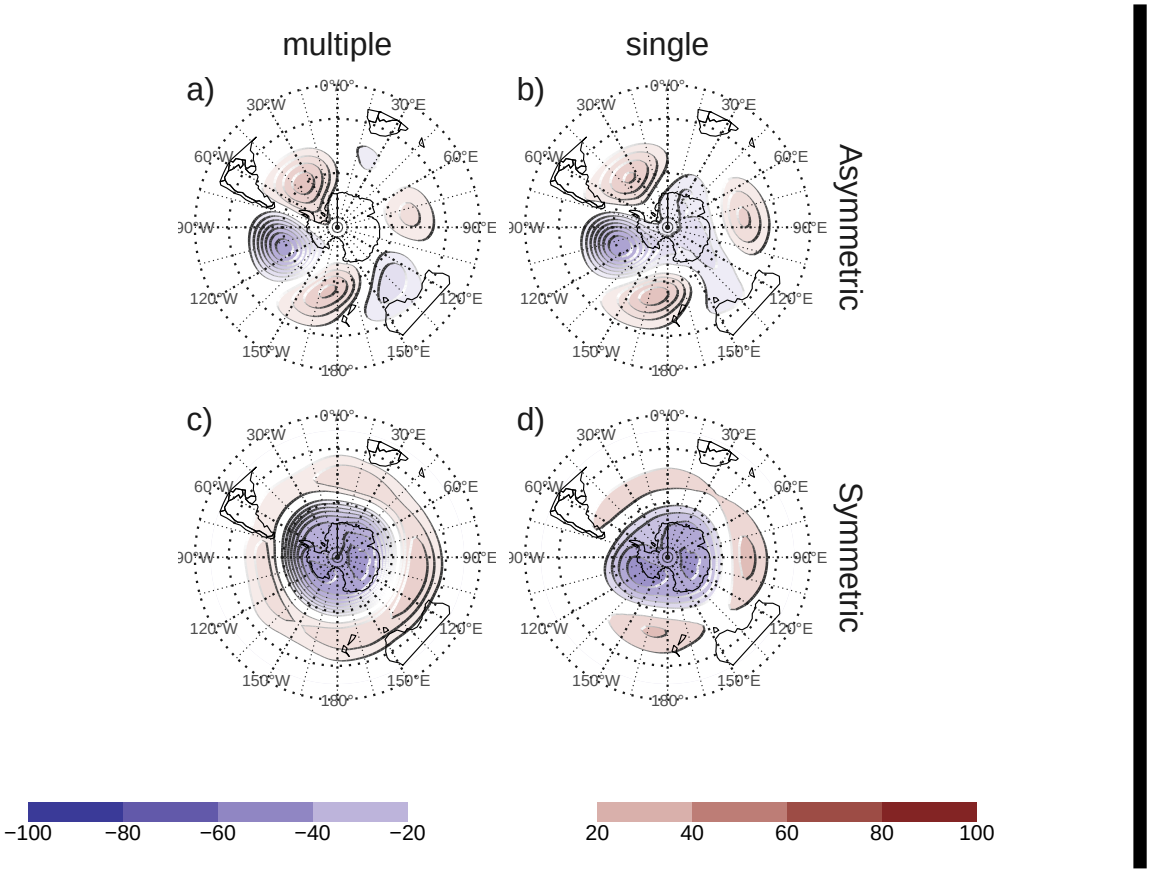

194 Fig. A6. Regressions maps resulting from performing one multiple regression (a. and b.) and from performing
195 two simple regressions (c. and d.)

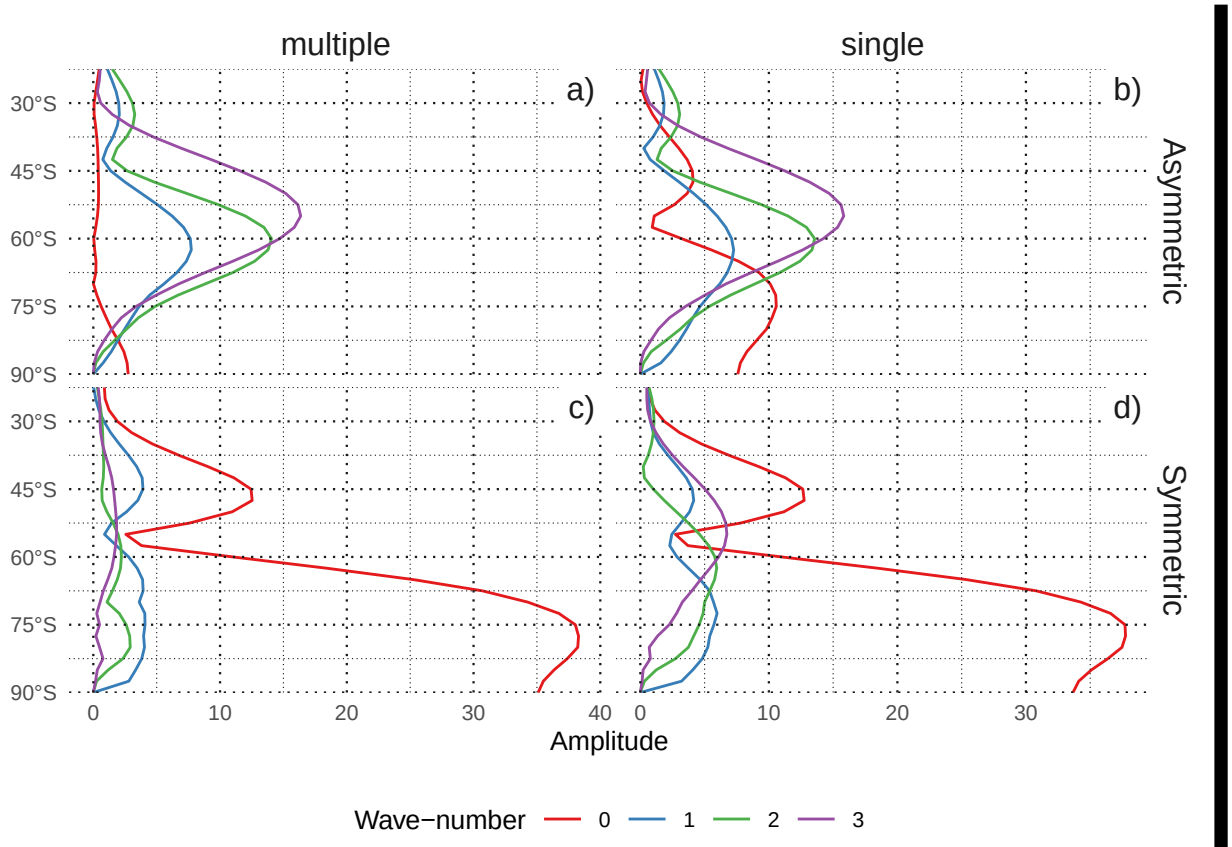
multiple
single
a)
b)
c)
d)
Asymmetric
Symmetric
30°S
45°S
60°S
75°S
90°S
0
10
20
30
40
Amplitude
Wave−number
0
1
2
3

Fig. A7.

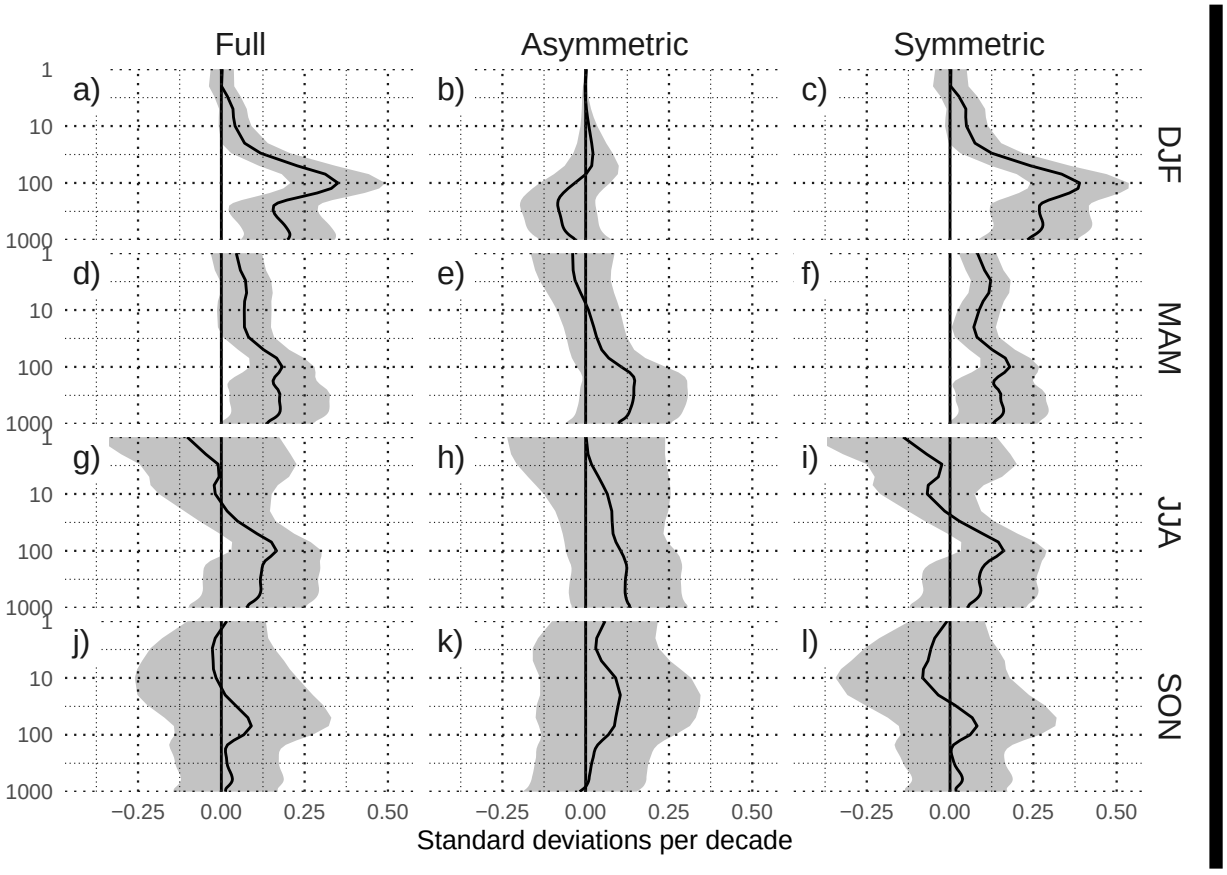

Fig. A8. Decadal trends of SAM indices for each season.